

Roles of pigment arrangement in light-harvesting  
phycobiliproteins revealed by recombinant  
techniques combined with two-dimensional  
electronic spectroscopy

*Masaaki Tsubouchi,<sup>1,2,\*</sup> Takatoshi Fujita,<sup>2</sup> Motoyasu Adachi,<sup>2</sup> and Ryuji Itakura<sup>1</sup>*

<sup>1</sup>Kansai Institute for Photon Science, National Institutes for Quantum Science and Technology  
(QST), 8-1-7 Umemidai, Kizugawa, Kyoto 619-0215, Japan

<sup>2</sup>Institute for Quantum Life Science, National Institutes for Quantum Science and Technology  
(QST), 4-9-1 Anagawa, Inage, Chiba 263-8555, Japan

**ABSTRACT:** We developed methods for protein synthesis and performed two-dimensional electronic spectroscopy (2D-ES) to examine the influence of pigment arrangement on the photoexcitation dynamics of light-harvesting proteins in phycobilisome. We synthesized allophycocyanin (APC), C-phycocyanin (CPC), and mutant CPC lacking the  $\beta$ 153 phycocyanobilin (PCB) pigment by an *Escherichia coli* expression system. The number of pigments in the mutant CPC is identical to that in the wild-type APC, and their spatial arrangements are similar. The absorption and fluorescence spectra of the mutant CPC closely resemble those of the wild-type CPC rather than the wild-type APC, indicating that pigment spatial arrangement is not a primary factor in determining the excited-state energy structure. The 2D-ES measurements show that the wild-type CPC retains broad positive signals at 1 ps, signifying incomplete relaxation and persistence of excited vibronic states, unlike APC, which vibrationally relaxes to the bottom of the potential energy surface within the same timeframe. The mutant CPC behaves similarly to the wild-type CPC in the 2D-ES, reinforcing that the pigment number or arrangement is not a dominant factor. Instead, the local pigment–protein interaction governs the electronic structure and relaxation dynamics. Structural analysis reveals that the bent structure of PCB in CPC’s  $\alpha$ -chain versus the planar structure of PCB in APC. The bent PCB in CPC reduces the degree of  $\pi$ -conjugation, and exhibits excited-state properties distinct from those of the planar structure of PCB in APC. This finding highlights a critical role of the electronic structure governed by the local interaction in ultrafast energy relaxation.

## INTRODUCTION

Phycobilisomes are large, highly organized light-harvesting protein complexes found in cyanobacteria and red algae, enabling efficient light harvesting in diverse aquatic environments.<sup>1</sup> Energy transfer in phycobilisomes is known to be unidirectional with an extremely high quantum efficiency close to unity.<sup>2</sup> Recent advances in cryo-electron microscopy (cryo-EM) have provided high-resolution structural insights into phycobilisomes, greatly enhancing our understanding of their architecture and the energy transfer mechanism.<sup>3-6</sup> Complementary studies using ultrafast spectroscopies have revealed details of energy transfer and quantum coherence after photo excitation, building on structural knowledge obtained from cryo-EM.<sup>7-10</sup> The phycobilisome complex is composed of multiple chromoproteins, primarily allophycocyanin (APC) and C-phycocyanin (CPC). Its core consists of APC assemblies, surrounded by CPC rods, with linker proteins connecting these components. Light energy absorbed by the phycobilisome is funneled toward the photosystem via the APC core. Within this energy transfer pathway, CPC and APC act as energy donors and acceptors, respectively.

Figures 1(a) and (b) show the structure and pigment arrangement of the APC trimer and CPC trimer, respectively, used in this study. Each APC monomer comprises  $\alpha$  and  $\beta$  subunits, which contain phycocyanobilin (PCB) pigments covalently bonded to cysteine residues at positions  $\alpha84$  and  $\beta84$ , respectively. In the APC trimer, the  $\alpha84$  PCB and  $\beta84$  PCB pigments from adjacent monomers are positioned in close proximity with the distance of around 2.1 nm.<sup>11</sup> In contrast, the CPC monomer contains a  $\beta153$  PCB pigment in addition to  $\alpha84$  PCB and  $\beta84$  PCB pigments. When a neighboring pair of  $\alpha84$  PCB and  $\beta84$  PCB pigments is photoexcited, excitonic states can form through excitonic coupling their electronically excited states. The  $\beta153$  PCB pigment, however, remains decoupled from this pair, and its energy level of the electronic excited state is

estimated to be higher than those of the excitonic states.<sup>12</sup> Delocalization of the electronic wave function across both  $\alpha$ 84 PCB and  $\beta$ 84 PCB, driven by excitonic coupling, is thought to facilitate the unidirectional flow of energy, which has been extensively examined through both experimental and theoretical studies.<sup>12-27</sup>

As shown in Figs. 1(a) and (b), the primary structure difference between APC and CPC is the absence or the presence of the  $\beta$ 153 PCB pigment. Although the  $\beta$ 153 PCB pigment is electronically decoupled from the  $\alpha$ 84 PCB and  $\beta$ 84 PCB pair, the photoexcitation dynamics differ remarkably between APC and CPC.<sup>27</sup> Investigating the molecular structure and spatial arrangement of pigments underlying this difference is crucial for understanding why nature has evolved phycobilisomes in their present form. Such insight could also guide the artificial design of antenna complexes with properties that surpass those found in nature. For this purpose, we have established methods for the artificial synthesis of light-harvesting proteins and developed a powerful tool for probing their ultrafast dynamics, that is, time-resolved two-dimensional electronic spectroscopy (2D-ES).<sup>27, 28</sup>

In this paper, we first describe methods used to artificially synthesize the APC and CPC trimers that constitute the phycobilisome of *Thermosynechococcus elongatus* BP-1 and to determine their molecular structures. Additionally, we synthesized a mutant CPC lacking the  $\beta$ 153 PCB pigment to compare its photoexcitation dynamics with those of the wild-type APC and CPC trimers. As shown in Fig. 1(c), the number of pigments in the mutant CPC is identical to that in the wild-type APC, and their spatial arrangements are also similar. If the spatial arrangement of pigments primarily governs the photoexcitation dynamics, the mutant CPC should exhibit photoexcitation dynamics resembling that of the wild-type of APC rather than the wild-type CPC. Next, we introduce a newly developed analysis method for the two-dimensional

electronic spectra obtained by 2D-ES, which enables a clear separation of the spectra into kinetics component and coherent dynamics. The 2D-ES has been employed to simultaneously probe energy relaxation kinetics and coherent dynamics resulting from photoexcitation to various vibronic states of light-harvesting proteins by ultrashort laser pulses with a broadband spectrum.<sup>29-40</sup> Despite its potential, the analysis has been challenging because multiple contributions are intricately mixed within the three-dimensional dataset measured by 2D-ES:  $S(E_{\text{exc}}, E_{\text{det}}, T)$ , where  $E_{\text{exc}}$ ,  $E_{\text{det}}$  and  $T$  are the excitation and detection energies, and the delay time after photoexcitation, respectively. Subsequently, we present the kinetics and coherent dynamics derived from the three proteins introduced earlier and compare their behaviors. Finally, we discuss the significance of pigment spatial arrangement in light-harvesting proteins and conclude with perspectives for future research.

## SAMPLE PREMARATION

The light-harvesting proteins APC and CPC were designed on the basis of the structure determined by cryo-EM<sup>6</sup> and were independently produced by an *Escherichia coli* (*E. coli*) expression system. APC and CPC proteins typically assemble into hexameric structures of heterodimers of  $\alpha$ - and  $\beta$ -chains within the phycobilisome supercomplex. To facilitate spectroscopic and biochemical experiments, we introduced mutations at the intertrimeric interface to ensure trimer formation. This point is the primary difference compared with our previous study.<sup>27</sup>

The recombinant *E. coli* strains and plasmids used in this study are presented in Fig. 1(d) and Supplementary Table S1, respectively. Two plasmids, pACYC\_HO1PcyA and pCDF\_MTSEF, were used for coexpression to enable pigment synthesis and protein modification, respectively.

The culture conditions for recombinant *E. coli* and the protein purification were identical to those previously described.<sup>27</sup> Specifically, Gly21 and Gly29 in the  $\alpha$ -chains of APC and CPC were substituted with arginine residues to introduce steric hinderances on the hexamer formation. Furthermore, to match the pigment configuration of CPC to that of APC, we generated a mutant CPC lacking the  $\beta$ 153 PCB pigment by substituting Cys153 with a tyrosine residue. Although substitution of the cysteine residue with any other amino acid results in loss of PCB, the tyrosine residue is thought to partially occupy the space left by the PCB's absence in its surrounding environment. In the following, unless otherwise specified, APC and CPC refer to the APC trimer and the CPC trimer, respectively. The mutant CPC refers to the  $\beta$ 153-deficient CPC.

To confirm the polypeptides present in the purified proteins, APC, CPC, and mutant CPC were analyzed by sodium dodecyl sulfate–polyacrylamide gel electrophoresis (SDS-PAGE). Figure 1(e) shows a photo of a stained gel. Two polypeptide bands corresponding to ApcA and ApcB appeared as a single band due to their similar migrations, while distinct bands for CpcA and CpcB were clearly observed. To further verify the presence of polypeptides and assess post-translational modification, intact protein mass spectroscopy was performed. The measured masses for pigment-bound polypeptides were as follows: 18093.1 Da for ApcA and 19,822.0 Da for ApcB in wild-type APC, 18,158.0 Da for CpcA and 21,436.7 Da for CpcB in wild-type CPC, and 18,158.0 Da for CpcA and 20,910.1 Da for CpcB in mutant CPC. This analysis indicates that PCB is covalently attached to both the  $\alpha$ - and  $\beta$ -chains, consistent with natural proteins purified from cyanobacteria. Furthermore, the  $\beta$ 153 PCB is absent in the mutant CPC. Additionally, their molecular masses are consistent with the design that CpcM catalyzed methylation of asparagine residues in the  $\beta$ -chain. To examine the molecular assembly, the purified proteins, APC, CPC, and mutant CPC were analyzed by size-exclusion column chromatography (Fig. 1(f)). The major

peaks for all three proteins appeared slightly after the 134 kDa marker, corresponding to the expected trimetric structure (approximately 110 kDa) formed by heterodimers of the  $\alpha$ - and  $\beta$ -chains. These results indicate that all three proteins form trimers with the designed post-translational modifications.

For the 2D-ES measurement, proteins were diluted in buffer containing 10% (w/v) glycerol and 10 mM NaCl to achieve a concentration of approximately 40  $\mu$ M (4.0 to 4.5 mg/mL). The solution was circulated through a sample cell with 1 mm-thick quartz windows and an optical path length of 0.2 mm using a peristaltic pump. The optical density of the absorption peak was approximately 0.4, as shown in Fig. 2.

## RESULTS

### Absorption and fluorescence spectra

The absorption spectra of the light-harvesting proteins synthesized in this study are shown in Fig. 2 as solid lines. The intensities are normalized at a wavelength of 278 nm, corresponding to the peak assigned to cysteine residues present in all three proteins in equal amounts. The spectrum of APC exhibits a peak and a shoulder at 650 nm and 615 nm, which have been assigned to the lower and higher excitonic states, respectively.<sup>15</sup> On the other hand, the spectrum of CPC does not clearly exhibit a shoulder, but it has a tail on the short-wavelength side. The peak wavelength is 620 nm which is 30 nm shorter than that of APC.

Despite the similar pigment arrangement of the wild-type APC and mutant CPC, the absorption spectrum of the mutant CPC resembles that of the wild-type CPC rather than that of APC. This result suggests that the spatial arrangement of the pigment molecules is not a significant factor in determining the energy structure of the electronically excited states. The

absorption intensity of the mutant CPC on the short-wavelength side is weaker than the wild-type, suggesting that the short-wavelength side corresponds to absorption by the  $\beta$ 153 pigments. When the contribution of the  $\beta$ 153 pigments is removed, a small shoulder becomes apparent around 575 nm in the mutant CPC spectrum. These absorption spectra are fitted using double Gaussian profiles to determine the wavelengths of the peak and shoulder components, which are listed in Table 1. Because the wild-type CPC contains three types of PCBs, its absorption spectrum should ideally be fitted with triple Gaussian profiles. However, the peak corresponding to  $\beta$ 153 PCBs cannot be clearly distinguished from the higher excitonic state formed by the  $\alpha$ 84- $\beta$ 84 pigment pairs; therefore, a double Gaussian profile is used. The shoulder component appears at approximately  $900\text{ cm}^{-1}$  higher energy than the main peak component. This result suggests that the energy differences between the excitonic states are similar across the three protein molecules.

The fluorescence spectra are shown in Fig. 2 as dashed lines, and the peak wavelength in these spectra are listed in Table 1. The Stokes shift of APC is  $190\text{ cm}^{-1}$ , which is about half of those of both the wild-type and mutant CPCs. The most notable feature is that the fluorescence spectrum of the mutant CPC is almost identical to that of the wild-type CPC. This indicates that the photon energy absorbed by the  $\beta$ 153 pigments of CPC is transferred to the excitonic states of the pigment pairs and subsequently relaxes to the bottom of the potential energy surface corresponding to the lower excitonic state before the spontaneous emission. The absence of  $\beta$ 153 PCB contribution to the fluorescence spectrum was previously discussed by Womick and Moran.<sup>12</sup> The present study provides clear confirmation of their interpretation through a comparative analysis of wild-type and mutant CPCs.

## Two-dimensional electronic spectra of APC: separation between contributions of kinetics and coherent dynamics

This subsection describes a newly developed 2D-ES analysis designed to separate the kinetic component and the coherent dynamics and to visualize the vibrational wave packet. Here, we present the photoinduced dynamics of APC. Figures 3(a), (b), and (c) show a series of two-dimensional electronic (2D-E) spectra  $S(E_{\text{exc}}, E_{\text{det}}; T)$  of APC. The horizontal and vertical axes show the excitation ( $E_{\text{exc}}$ ) and detection ( $E_{\text{det}}$ ) energies, respectively.  $T$  is the delay time after photoexcitation. Positive amplitudes indicate increased transmission, corresponding to the ground state bleaching (GSB) or the stimulated emission (SE), while negative amplitudes indicate the excited state absorption (ESA). At the moment of the excitation ( $T = 0$  fs), the signal appears along the diagonal, indicating that APC is detected at the same energy as the excitation energy before any energy relaxation occurs. At  $T = 1$  ps, the amplitude distribution in the 2D-E spectrum becomes aligned parallel to the horizontal axis at  $E_{\text{det}} = 15,240 \text{ cm}^{-1}$ , which is close to the peak of the fluorescence spectrum of APC ( $15,200 \text{ cm}^{-1}$ ) shown in Fig. 2. This suggests that all the excited vibronic states populated by the pump pulses have nearly completely relaxed to the bottom of the potential energy surface of the lower excitonic states.

A series of 2D-E spectra  $S(E_{\text{exc}}, E_{\text{det}}; T)$  is reconfigured into a series of transient spectra obtained by slicing the three-dimensional data set of  $S(E_{\text{exc}}, E_{\text{det}}, T)$  at specific excitation energies. Figure 3(d) shows the transient spectrum of APC at  $E_{\text{exc}} = 16,670 \text{ cm}^{-1}$  corresponding to the shoulder in the absorption spectrum. The dynamic Stokes shift rapidly completes within 1 ps, and the detection energy converges to  $E_{\text{det}} = 15,250 \text{ cm}^{-1}$ . In contrast, the transient spectrum in Fig. 3(g) obtained at  $E_{\text{exc}} = 15,550 \text{ cm}^{-1}$  which is  $170 \text{ cm}^{-1}$  higher than the absorption peak,

exhibits not only the dynamic Stoke shift but also the oscillation of the peak detection energy clearly in the time-dependent transient spectrum.

To understand the kinetics of the photoexcited molecules, Global analysis has been widely applied to the transient spectra. However, when coherent features overlap with kinetic components, applying Global analysis becomes difficult, because the experimental data cannot be accurately reconstructed using a small number of principal components obtained through singular value decomposition.<sup>41, 42</sup> Therefore, the time profiles obtained at all pairs of excitation and detection energies are fitted with a single exponential function,

$$S(T; E_{\text{exc}}, E_{\text{det}}) = A_0 + A_1 \exp(-T/\tau_1), \quad (1)$$

where  $\tau_1$  is the time constant of the single exponential decay, and  $A_0$  and  $A_1$  are the amplitudes of the constant and the decay components, respectively. These three parameters are the functions of  $E_{\text{exc}}$  and  $E_{\text{det}}$ . The kinetic component and coherent dynamics are then separated based on the fitted profiles and their residuals, respectively. Further details are provided in Supplementary Sec. 2. Figures 3(e) and (f) display the kinetic and residual (coherent) components, respectively, obtained by decomposing the transient spectrum measured at  $E_{\text{exc}} = 16,670 \text{ cm}^{-1}$  shown in Fig. 3(d). Residual signals are seen along the detection energy around  $E_{\text{det}} = 15,250 \text{ cm}^{-1}$ . However, the temporal profile of this component cannot be consistently reproduced across multiple experiments within the signal to noise limitation of our apparatus. Consequently, the coherent component is associated with excitation to the shoulder in the absorption spectrum is not further discussed in this paper. The decomposition of the transient spectrum measured at  $E_{\text{exc}} = 15,550 \text{ cm}^{-1}$  is presented in Figs. 3(h) and (i). The pronounced beating feature is evident in the residual component, exhibiting a node around the detection energy of  $E_{\text{det}} = 15,250 \text{ cm}^{-1}$ . The sign of the amplitude reverses at the node, corresponding to a  $\pi$  phase shift in the beating pattern. This

provides clear evidence of vibrational wave packet motion on the electronically excited state, as discussed later.

Figures 4(a), (b), and (c) illustrate two-dimensional maps of the parameters  $A_0$ ,  $A_1$ , and  $\tau_1$ , respectively, obtained through least-squares fitting of Eq. (1) to the observed time-profiles  $S(T; E_{\text{exc}}, E_{\text{det}})$ . These summarize the kinetic information of photo-excited APC. The constant component  $A_0$  closely resembles the 2D-E spectrum (Fig. 3(c)) measured at a delay time of  $T = 1$  ps, suggesting that vibrational relaxation in the electronically excited state of APC is completed within 1 ps. Black and white dots appear in the 2D maps, particularly around the detection energy of  $E_{\text{det}} \sim 15,400 \text{ cm}^{-1}$ . These indicate that the fitting does not converge well, because the observed time profiles lack any noticeable decay or rise features. The parameter  $A_1$  exhibits a positive amplitude in the detection energy higher than  $E_{\text{det}} \sim 15,400 \text{ cm}^{-1}$  and a negative amplitude in the detection energy lower than that energy. A positive  $A_1$  indicates that the population at the corresponding detection energy decays, whereas a negative  $A_1$  indicates population growth. The boundary is located around  $E_{\text{det}} = 15,400 \text{ cm}^{-1}$ , corresponding to the peak of the absorption spectrum of APC.

The 2D-map of the decay time-constant  $\tau_1$  shown in Fig. 4(c) consists of two components. One is a fast decay component ( $\tau_1 < 200 \text{ fs}$ ) along the diagonal, indicating that the detected quantum states correspond to those populated just after photoexcitation. The other is a relatively slow decay or rise component ( $\tau_1 \sim 500 \text{ fs}$ ) located below the diagonal. These findings suggest dynamics of photoexcited APC involving fast internal conversion between the excitonic states, followed by vibrational energy relaxation to the bottom of the potential energy surface of the electronically excited state.<sup>13-15, 18</sup> Figure 4(d) summarizes the detection-energy dependence of the decay (or rise) time-constants. At detection energies close to the excitation energy, the time

constant is a few tens of femtoseconds, and it rapidly increases to approximately 500 fs as the detection energy decreases.

Next, we consider the coherent nature of the photoexcited APC. The detailed method for coherence analysis is provided in Supplementary Sec. 3. The beat frequency spectrum obtained at the excitation energy  $E_{\text{exc}} = 15,550 \text{ cm}^{-1}$  is shown in Fig. 5(a). We found the peak beat frequency is  $\nu_{\text{beat}} = 202 \text{ cm}^{-1}$  and the full width at half maximum  $46 \text{ cm}^{-1}$ . The broad width of the peak indicates the short decoherence time on the order of a few hundred femtoseconds. The beat spectra were calculated for all pairs of excitation and detection energies  $(E_{\text{exc}}, E_{\text{det}})$ , and the intensities at  $\nu_{\text{beat}} = 202 \text{ cm}^{-1}$  in the beat spectrum are plotted as a two-dimensional map, as shown in Fig. 5(b). The two peaks are exhibited with a nodal line running parallel to the excitation energy axis around the detection energy of  $E_{\text{det}} = 15,250 \text{ cm}^{-1}$ . In Fig. 5(b), the contour map of the 2D-E spectrum observed at  $T = 1 \text{ ps}$  is overlaid to the beat intensity map. The maximum beat intensity occurs at an excitation energy of  $E_{\text{exc}} = 15,550 \text{ cm}^{-1}$  which is  $170 \text{ cm}^{-1}$  higher than the absorption peak. The nodal line of the beat intensity map follows the ridge of the 2D-E spectrum, corresponding to the bottom of the potential energy surface of the electronically excited states. Figure 5(c) presents the spectra of the beat intensity and phase of the beating time profiles at an excitation energy of  $E_{\text{exc}} = 15,550 \text{ cm}^{-1}$  as a function of detection energy. In the phase spectrum, a clear  $\pi$ -phase jump is observed at the detection energy of  $E_{\text{det}} = 15,250 \text{ cm}^{-1}$ , corresponding to the nodal line in the 2D map. These results provide evidence for the formation of a vibrational wave packet on the electronically excited state, as illustrated in Fig. 5(d).<sup>7</sup> The components of A and B indicated in Figs. 5(b) and (c) correspond to the turning points on the potential energy surface of the vibrational wave packet. The decoherence time of the beating signal as a function of detection energy is overlayed in the beating spectrum in Fig. 5(c). Around

the detection energy of  $E_{\text{det}} = 15,250 \text{ cm}^{-1}$ , the fitting results of the decoherence time is not reliable, because the beat intensity is too weak to fit to the oscillating model function. The decoherence time at the high detection energies is  $140 \pm 20 \text{ fs}$ , on the other hand, that at the low energies is  $370 \pm 80 \text{ fs}$ . These decoherence times are much longer than the decay time-constant  $\tau_1$  shown in Fig. 4(d). This suggests that decoherence of vibrational wave packet around the bottom of the potential energy surface is slower than vibrational energy relaxation from higher vibronic states.

### Wild-type and $\beta$ 153 deficient CPCs

A series of 2D-E spectra of the CPC energy-donor protein is shown in Figs. 6(a-c). The positive signals spanning a broad detection-energy range higher than  $15,270 \text{ cm}^{-1}$  are detected at  $T = 1 \text{ ps}$ , unlike in the case of APC. This result indicates that relaxation to the bottom of the potential is not completed and, therefore, the excited vibronic states still survive at picosecond time delays after the excitation. The ESA component also appears at a detection energy below  $E_{\text{det}} < 15,270 \text{ cm}^{-1}$ , which is not clearly seen in the case of APC. As seen in Fig. 1(a) and (b), both APC and CPC have similar structures, except for the  $\beta$ 153 pigments existing in CPC. Nevertheless, the absorption spectrum and the energy relaxation kinetics of CPC are found to be far different from those of APC. This difference might be related to the efficient energy transfer in phycobilisomes.<sup>19</sup>

Figures 6(d-f) present the 2D-E spectra of the mutant CPC lacking the  $\beta$ 153 pigments. The series of the 2D-E spectra looks more closely resembles that of the wild-type CPC than the wild-type of APC. This tendency is consistent with the absorption spectra. To enable a quantitative comparison of the 2D-E spectra, Fig. 7 summarizes the transient spectra of the wild-type CPC,

mutant CPC, and wild-type APC at a long delay time ( $T = 2$  ps), obtained by projecting the 2D-E spectra onto the detection energy axis. The spectrum of the mutant CPC differs remarkably from that of APC, while being nearly identical to that of the wild-type CPC, except for a red shift of approximately  $40\text{ cm}^{-1}$  and a weak dip around  $16,500\text{ cm}^{-1}$ .

Figure 8 compares the transient spectra  $S(E_{\text{det}}, T; E_{\text{exc}})$  of the wild-type CPC and the  $\beta 153$  deficient CPC. These spectra are obtained at the excitation energies  $E_{\text{exc}} = 16,330\text{ cm}^{-1}$  and  $16,200\text{ cm}^{-1}$  which are  $200\text{ cm}^{-1}$  higher than their respective absorption peaks. The transient spectra obtained at the higher excitation energy  $E_{\text{exc}} = 17,210\text{ cm}^{-1}$  are shown in Supplementary Sec. 4. In the transient spectra of CPC, the GSB or SE component with positive amplitude overlaps with the ESA component, which has a negative component, around  $15,300\text{ cm}^{-1}$ . Consequently, the time-constant obtained by fitting to Eq. (1) cannot be easily interpreted, and therefore, the fitting procedure is used solely to separate the coherent dynamics from the kinetic component. As seen in the kinetic component of wild-type CPC in Fig. 8(b), the energy of the initially excited state is rapidly redistributed among the vibronic states within 100 fs. Subsequently, this redistributed energy does not relax to the bottom of the potential energy surface on the electronically excited state within 2 ps. This can be seen by comparing the transient and fluorescence spectra shown in Fig. 7. Specifically, the transient spectrum of wild-type APC at  $T = 2$  ps is nearly identical to the fluorescence spectrum corresponding to the fully relaxed state. In contrast, the transient spectrum of the wild-type CPC is significantly broader than the fluorescence spectra. Figure 8(c) shows that the beating signal decays rapidly within a few femtoseconds, and the nodal line is not discernible.

These characteristics of the wild-type CPC differ significantly from those observed in the wild-type APC. On the other hand, as shown in Figs. 8(e) and (f), the kinetics component and

coherent dynamics of the  $\beta$ 153 deficient CPC are very similar to the wild-type CPC, rather than APC. The results obtained in this study indicate that the spatial arrangement of pigments is not a significant factor in determining the photo-induced dynamics of light-harvesting proteins. The effect of absence of the pigment covalently bonded to the Cys153 is simply the elimination of light absorption by the  $\beta$ 153 pigment and the associated energy transfer from it to the pigment pair formed by  $\alpha$ 84 and  $\beta$ 84.

Figure 9 compares the stereo structures of the pigment PCB in the wild-type APC and the wild-type CPC. The structures of  $\beta$ 84 PCB in APC and CPC appear similarly. In contrast, the  $\alpha$ 84 PCB in APC has a planar structure, whereas that in CPC is bent, as clearly seen in the side view of PCB highlighted by the red circle. This difference may be caused by a reduction in  $\pi$ -conjugation at the position indicated by the red circle in PCB. The structural change alters the electronic structure and, consequently, the photo-induced dynamics of APC compared to CPC. So far, investigations of energy transfer in phycobilisomes have focused on the distance and relative orientation between the pigment molecules, primarily through mechanisms such as fluorescence resonance energy transfer (FRET) and excitonic interactions. The present study suggests that local interactions – both between neighboring pigment molecules and between the piment and the surrounding amino acid residues – are also crucial for understanding the dynamics of energy transfer. These interactions influence the molecular structure of the pigments which is closely linked to their electronic properties.

## SUMMARY AND PERSPECTIVES

To investigate the effect of pigment arrangement in the light-harvesting proteins of phycobilisomes, we synthesized the wild-type APC and CPC and the mutant CPC lacking  $\beta$ 153

PCB, and applied 2D-ES. The number of pigments in the mutant CPC is identical to that in the wild-type APC, and their spatial arrangements are similar. Absorption spectra revealed that APC exhibits a peak at 650 nm with a shoulder at 615 nm, corresponding to lower and higher excitonic states, whereas CPC exhibited a peak at 620 nm without a distinct shoulder. The mutant CPC spectrum resembled that of wild-type CPC, rather than APC, indicating that pigment spatial arrangement does not primarily determine excited-state energy structure. In 2D-ES, wild-type CPC displayed broad positive signals above  $E_{\text{det}} = 15,270 \text{ cm}^{-1}$  at 1 ps, indicating incomplete relaxation and persistence of excited vibronic states, unlike APC, which fully relaxed to the bottom of the potential energy surface. Despite similar pigment spatial arrangement, APC and the mutant CPC lacking  $\beta 153$  PCB differ markedly in relaxation kinetics. The mutant CPC behaved similarly to the wild-type CPC in 2D-ES, reinforcing that pigment spatial arrangement is not a dominant factor. Structural analysis revealed bent PCB in CPC's  $\alpha$ -chain versus planar PCB in APC, likely reducing  $\pi$ -conjugation in CPC and altering its excited-state properties.

To further validate the structural elements that govern kinetics and coherence in light-harvesting proteins, we plan to synthesize the various mutant APC and CPC proteins. For example, certain mutations are designed to prevent the formation of excitonic states or disrupt the energy balance within these states. These future investigations will highlight a critical role of local pigment-protein and pigment-pigment interactions in ultrafast energy relaxation and coherence, offering valuable insights for the design of artificial light-harvesting systems with tailored dynamics.

## EXPERIMENTAL SECTION

### SDS-PAGE analysis

NuPAGE Bis-Tris Precast Gel (Thermo Fisher Scientific) and 2-(N-morpholino)ethanesulfonic acid buffer were used for electrophoresis analysis. Electrophoresis was performed at a constant voltage of 100 V for 80 min, and the gels were subsequently stained with EzStain AQua (ATTO).

### Mass spectrometry analysis

Purified protein samples were analyzed using an ultra-high-performance liquid chromatography system coupled to a quadrupole time-of-flight mass spectrometer (H-Class and Xevo G2-XS; Milford, MA, USA, Waters). Intact proteins were desalted via chromatographic separation on a MassPREP Micro Desalting Column (Waters) using a gradient from water to acetonitrile containing 0.1% formic acid. Leucine enkephalin and NaI were employed for quantifier ion and calibration, respectively. Raw data generated by MassLynx were processed using UNIFI version 1.9.

### Gel filtration analysis

A Superdex 200 10/300GL gel filtration column was equilibrated with Buffer T. A 0.03 mL sample at a concentration of 5  $\mu$ M was injected and eluted at a flow rate of 0.5 mL/min. Protein elution was monitored by measuring absorbance at 280 nm.

### Absorption and fluorescence spectroscopies

Absorption spectra were measured at room temperature (23 °C) by JASCO spectrophotometer V-760. Fluorescence spectra were measured by JASCO spectrofluorometer FP-8300.

## Two-dimensional electronic spectroscopy

The two-dimensional electronic spectra were measured using a previously reported setup.<sup>27</sup> The pump-probe configuration was employed in this study. An advantage of this configuration is that the absorptive 2D electronic spectra directly visualizing the transient behaviors can be obtained automatically with extremely high phase stability. In brief, we produced sub-10-femtosecond visible pulses using a Yb:KGW laser followed by two pulse-compression stages.<sup>28</sup> The coherent time interval between two pump pulses was scanned by the Translating-Wedge-Based Identical Pulses eNcoding System (TWINS)<sup>43, 44</sup> from  $-60$  to  $60$  fs in steps of  $0.4$  fs. The waiting time,  $T$ , was scanned from  $0$  to  $2000$  fs in steps of  $4$  fs. The energy density of the excitation pulse irradiating the sample was  $40 \mu\text{J}/\text{cm}^2$  in each pulse, which did not induce a non-linear response by a single pulse. At the sample position, the linear polarizations of the two laser pulses were set in parallel. The duration of the excitation pulses was  $13$  fs at the sample position. The spectral width was sufficient to excite the entire absorption spectrum of APC and CPC. One measurement, which collected around  $500$  2D-E spectra, was completed within three hours, and so multiple measurements with several proteins could be performed on the same day, indicating that quantitative comparison between different proteins is enabled.

## ASSOCIATED CONTENT

### Supporting Information.

The Supporting Information is available free of charge at xxxx.

Detailed information on sample preparation and the additional dataset (PDF).

## AUTHOR INFORMATION

### Corresponding Author

**Masaaki Tsubouchi** – Kansai Institute for Photon Science, National Institutes for Quantum Science and Technology (QST), 8-1-7 Umemidai, Kizugawa, Kyoto 619-0215, Japan;  
<https://orcid.org/0000-0003-1158-0867>; Email: [tsubouchi.masaaki@qst.go.jp](mailto:tsubouchi.masaaki@qst.go.jp)

### Authors

**Takatoshi Fujita** – Institute for Quantum Life Science, National Institutes for Quantum Science and Technology (QST), 4-9-1 Anagawa, Inage, Chiba 263-8555, Japan; <https://orcid.org/0000-0003-1504-2249>

**Motoyasu Adachi** – Institute for Quantum Life Science, National Institutes for Quantum Science and Technology (QST), 4-9-1 Anagawa, Inage, Chiba 263-8555, Japan;  
<https://orcid.org/0000-0003-2353-880X>

**Ryuji Itakura** – Kansai Institute for Photon Science, National Institutes for Quantum Science and Technology (QST), 8-1-7 Umemidai, Kizugawa, Kyoto 619-0215, Japan;  
<https://orcid.org/0000-0003-0508-4760>

## Notes

The authors declare no competing financial interest.

## ACKNOWLEDGMENT

We thank Yuji Kagotani and Takemi Kanazawa at QST for their assistances in performing the measurements of protein absorption and fluorescence spectra and in protein synthesis, respectively. We also thank Prof. A. Ishizaki at The University of Tokyo for valuable comments about 2D-ES. This research was supported by the MEXT Quantum Leap Flagship Program (JPMXS0120330644). We are grateful for the financial support of JSPS KAKENHI (JP21H01898) and the QST President's Strategic Grant (Exploratory Research). The mass spectrometry analysis shown in the Supplementary Materials was supported by J-PARC MLF deuteration laboratory.

## REFERENCES

(1) Gantt, E. Phycobilisomes: light-harvesting pigment complexes. *Bioscience* **1975**, *25*, 781–788.

(2) Blankenship, R. E. *Molecular mechanisms of photosynthesis*; Wiley, 2021.

(3) Zheng, L.; Zheng, Z.; Li, X.; Wang, G.; Zhang, K.; Wei, P.; Zhao, J.; Gao, N. Structural insight into the mechanism of energy transfer in cyanobacterial phycobilisomes. *Nat. Commun.* **2021**, *12*, No. 5497.

(4) Ma, J.; You, X.; Sun, S.; Wang, X.; Qin, S.; Sui, S. F. Structural basis of energy transfer in porphyrinidium purpureum phycobilisome. *Nature* **2020**, *579*, 146–151.

(5) Domínguez-Martín, M. A.; Sauer, P. V.; Kirst, H.; Sutter, M.; Bína, D.; Greber, B. J.; Nogales, E.; Polívka, T.; Kerfeld, C. A. Structures of a phycobilisome in light-harvesting and photoprotected states. *Nature* **2022**, *609*, 835–845.

(6) Kawakami, K.; Hamaguchi, T.; Hirose, Y.; Kosumi, D.; Miyata, M.; Kamiya, N.; Yonekura, K. Core and rod structures of a thermophilic cyanobacterial light-harvesting phycobilisome. *Nat. Commun.* **2022**, *13*, No. 3389.

(7) Sil, S.; Tilluck, R. W.; Mohan, T. M. N.; Leslie, C. H.; Rose, J. B.; Domínguez-Martín, M. A.; Lou, W.; Kerfeld, C. A.; Beck, W. F. Excitation energy transfer and vibronic coherence in intact phycobilisomes. *Nat. Chem.* **2022**, *14*, 1286–1294.

(8) Sohoni, S.; Lloyd, L. T.; Hitchcock, A.; MacGregor-Chatwin, C.; Iwanicki, A.; Ghosh, I.; Shen, Q.; Hunter, C. N.; Engel, G. S. Phycobilisome's exciton transfer efficiency relies on an

energetic funnel driven by chromophore–linker protein interactions. *J. Am. Chem. Soc.* **2023**, *145*, 11659–11668.

(9) Navotnaya, P.; Sohoni, S.; Lloyd, L. T.; Abdulhadi, S. M.; Ting, P. C.; Higgins, J. S.; Engel, G. S. Annihilation of excess excitations along phycocyanin rods precedes downhill flow to allophycocyanin cores in the phycobilisome of *synechococcus elongatus* PCC 7942. *J. Phys. Chem. B* **2022**, *126*, 23–29.

(10) Hirota, Y.; Serikawa, H.; Kawakami, K.; Ueno, M.; Kamiya, N.; Kosumi, D. Ultrafast energy transfer dynamics of phycobilisome from *thermosynechococcus vulcanus*, as revealed by ps fluorescence and fs pump-probe spectroscopies. *Photosynth. Res.* **2021**, *148*, 181–190.

(11) Brejc, K.; Ficner, R.; Huber, R.; Steinbacher, S. Isolation, crystallization, crystal structure analysis and refinement of allophycocyanin from the cyanobacterium *Spirulina platensis* at 2.3 Å resolution. *J. Mol. Biol.* **1995**, *249*, 424–440.

(12) Womick, J. M.; Moran, A. M. Nature of excited states and relaxation mechanisms in C-phycocyanin. *J. Phys. Chem. B* **2009**, *113*, 15771–15782.

(13) Edington, M. D.; Riter, R. E.; Beck, W. F. Evidence for coherent energy transfer in allophycocyanin trimers. *J. Phys. Chem.* **1995**, *99*, 15699–15704.

(14) Edington, M. D.; Riter, R. E.; Beck, W. F. Interexciton-state relaxation and exciton localization in allophycocyanin trimers. *J. Phys. Chem. B* **1996**, *100*, 14206–14217.

(15) Edington, M. D.; Riter, R. E.; Beck, W. F. Femtosecond transient hole-burning detection of interexciton-state radiationless decay in allophycocyanin trimers. *J. Phys. Chem. B* **1997**, *101*, 4473–4477.

(16) Homoeelle, B. J.; Edington, M. D.; Diffey, W. M.; Beck, W. F. Stimulated photon-echo and transient-grating studies of protein-matrix solvation dynamics and interexciton-state radiationless decay in  $\alpha$  phycocyanin and allophycocyanin. *J. Phys. Chem. B* **1998**, *102*, 3044-3052.

(17) Zhang, J. M.; Shiu, Y. J.; Hayashi, M.; Liang, K. K.; Chang, C. H.; Gulbinas, V.; Yang, C. M.; Yang, T. S.; Wang, H. Z.; Chen, Y. T.; et al. Investigations of ultrafast exciton dynamics in allophycocyanin trimer. *J. Phys. Chem. A* **2001**, *105*, 8878-8891.

(18) Womick, J. M.; Moran, A. M. Exciton coherence and energy transport in the light-harvesting dimers of allophycocyanin. *J. Phys. Chem. B* **2009**, *113*, 15747-15759.

(19) Womick, J. M.; Miller, S. A.; Moran, A. M. Toward the origin of exciton electronic structure in phycobiliproteins. *J. Chem. Phys.* **2010**, *133*, No. 024507.

(20) Womick, J. M.; Moran, A. M. Vibronic enhancement of exciton sizes and energy transport in photosynthetic complexes. *J. Phys. Chem. B* **2011**, *115*, 1347-1356.

(21) Womick, J. M.; West, B. A.; Scherer, N. F.; Moran, A. M. Vibronic effects in the spectroscopy and dynamics of *C*-phycocyanin. *J. Phys. B: At. Mol. Opt. Phys.* **2012**, *45*, No. 154016.

(22) Fălămaș, A.; Porav, S. A.; Tosa, V. Investigations of the energy transfer in the phycobilisome antenna of *arthrospira platensis* using femtosecond spectroscopy. *Appl. Sci.* **2020**, *10*, No. 4045.

(23) Zhu, R.; Li, W.; Zhen, Z.; Zou, J.; Liao, G.; Wang, J.; Wang, Z.; Chen, H.; Qin, S.; Weng, Y. Quantum phase synchronization via exciton-vibrational energy dissipation sustains long-lived coherence in photosynthetic antennas. *Nat. Commun.* **2024**, *15*, No. 3171.

(24) Moya, R.; Norris, A. C.; Kondo, T.; Schlau-Cohen, G. S. Observation of Robust Energy Transfer in the Photosynthetic Protein Allophycocyanin Using Single-Molecule Pump-Probe Spectroscopy. *Nat. Chem.* **2022**, *14*, 153-159.

(25) Wu, P.-J. E.; Sohoni, S.; Engel, G. S. Vibrational Relaxation Completes the Excitation Energy Transfer and Localization of Vibronic Excitons in Allophycocyanin  $\alpha$ 84- $\beta$ 84. *J. Phys. Chem. Lett.* **2024**, *15*, 11577-11586.

(26) Sohoni, S.; Wu, P.-J. E.; Shen, Q.; Lloyd, L. T.; MacGregor-Chatwin, C.; Hitchcock, A.; Engel, G. S. Resonant Vibrational Enhancement of Downhill Energy Transfer in the C-Phycocyanin Chromophore Dimer. *J. Phys. Chem. Lett.* **2024**, *15*, 11569-11576.

(27) Tsubouchi, M.; Ishii, N.; Fujita, T.; Adachi, M.; Itakura, R. Dependence of energy relaxation and vibrational coherence on the location of light-harvesting chromoproteins in photosynthetic antenna protein complexes. *J. Chem. Phys.* **2025**, *162*, No. 145102.

(28) Tsubouchi, M.; Ishii, N.; Kagotani, Y.; Shimizu, R.; Fujita, T.; Adachi, M.; Itakura, R. Beat-frequency-resolved two-dimensional electronic spectroscopy: disentangling vibrational coherences in artificial fluorescent proteins with sub-10-fs visible laser pulses. *Opt. Express* **2023**, *31*, 6890-6906.

(29) Mukamel, S. Multidimensional femtosecond correlation spectroscopies of electronic and vibrational excitations. *Annu. Rev. Phys. Chem.* **2000**, *51*, 691-729.

(30) Hybl, J. D.; Ferro, A. A.; Jonas, D. M. Two-dimensional Fourier transform electronic spectroscopy. *J. Chem. Phys.* **2001**, *115*, 6606-6622.

(31) Jonas, D. M. Two-dimensional femtosecond spectroscopy. *Annu. Rev. Phys. Chem.* **2003**, *54*, 425-463.

(32) Mančal, T.; Pisliakov, A. V.; Fleming, G. R. Two-dimensional optical three-pulse photon echo spectroscopy. I. Nonperturbative approach to the calculation of spectra. *J. Chem. Phys.* **2006**, *124*, No. 234504.

(33) Pisliakov, A. V.; Mančal, T.; Fleming, G. R. Two-dimensional optical three-pulse photon echo spectroscopy. II. Signatures of coherent electronic motion and exciton population transfer in dimer two-dimensional spectra. *J. Chem. Phys.* **2006**, *124*, No. 234505.

(34) Turner, D. B.; Wilk, K. E.; Curmi, P. M. G.; Scholes, G. D. Comparison of electronic and vibrational coherence measured by two-dimensional electronic spectroscopy. *J. Phys. Chem. Lett.* **2011**, *2*, 1904-1911.

(35) Ishizaki, A.; Fleming, G. R. Quantum coherence in photosynthetic light harvesting. *Annu. Rev. Condens. Matter Phys.* **2012**, *3*, 333-361.

(36) Oliver, T. A. A. Recent advances in multidimensional ultrafast spectroscopy. *R. Soc. Open Sci.* **2018**, *5*, No. 171425.

(37) Gelzinis, A.; Augulis, R.; Butkus, V.; Robert, B.; Valkunas, L. Two-dimensional spectroscopy for non-specialists. *Biochim. Biophys. Acta* **2019**, *1860*, 271-285.

(38) Cao, J.; Cogdell, R. J.; Coker, D. F.; Duan, H.-G.; Hauer, J.; Kleinekathöfer, U.; Jansen, T. L. C.; Mančal, T.; Miller, R. J. D.; Ogilvie, J. P.; et al. Quantum biology revisited. *Sci. Adv.* **2020**, 6, No. eaaz4888.

(39) Romero, E.; Novoderezhkin, V. I.; van Grondelle, R. Quantum design of photosynthesis for bio-inspired solar-energy conversion. *Nature* **2017**, 543, 355-365.

(40) Scholes, G. D.; Fleming, G. R.; Chen, L. X.; Aspuru-Guzik, A.; Buchleitner, A.; Coker, D. F.; Engel, G. S.; van Grondelle, R.; Ishizaki, A.; Jonas, D. M.; et al. Using coherence to enhance function in chemical and biophysical systems. *Nature* **2017**, 543, 647-656.

(41) van Stokkum, I. H. M.; Jumper, C. C.; Snellenburg, J. J.; Scholes, G. D.; van Grondelle, R.; Malý, P. Estimation of damped oscillation associated spectra from ultrafast transient absorption spectra. *J. Chem. Phys.* **2016**, 145, No. 174201.

(42) van Stokkum, I. H. M.; Kloz, M.; Polli, D.; Viola, D.; Weißenborn, J.; Peerbooms, E.; Cerullo, G.; Kennis, J. T. M. Vibronic dynamics resolved by global and target analysis of ultrafast transient absorption spectra. *J. Chem. Phys.* **2021**, 155, No. 114113.

(43) Brida, D.; Manzoni, C.; Cerullo, G. Phase-locked pulses for two-dimensional spectroscopy by a birefringent delay line. *Opt. Lett.* **2012**, 37, 3027-3029.

(44) Réhault, J.; Maiuri, M.; Oriana, A.; Cerullo, G. Two-dimensional electronic spectroscopy with birefringent wedges. *Rev. Sci. Instrum.* **2014**, 85, No. 123107.

**Table 1.** Spectroscopic data of APC, CPC, and the  $\beta$ 153 deficient CPC (mutant CPC). The wavelengths of the peak and the shoulder of absorption spectra are determined by fitting of the spectra to the double Gaussian functions.

	Abs. peak	Abs. shoulder	<sup>a</sup> Difference	Fluor. peak	Stokes shift
APC	650 nm	615 nm	880 $\text{cm}^{-1}$	658 nm	190 $\text{cm}^{-1}$
CPC	620 nm	586 nm	940 $\text{cm}^{-1}$	638 nm	460 $\text{cm}^{-1}$
Mutant CPC	625 nm	592 nm	890 $\text{cm}^{-1}$	639 nm	350 $\text{cm}^{-1}$

<sup>a</sup> Energy difference between the peak and shoulder of the absorption spectra.

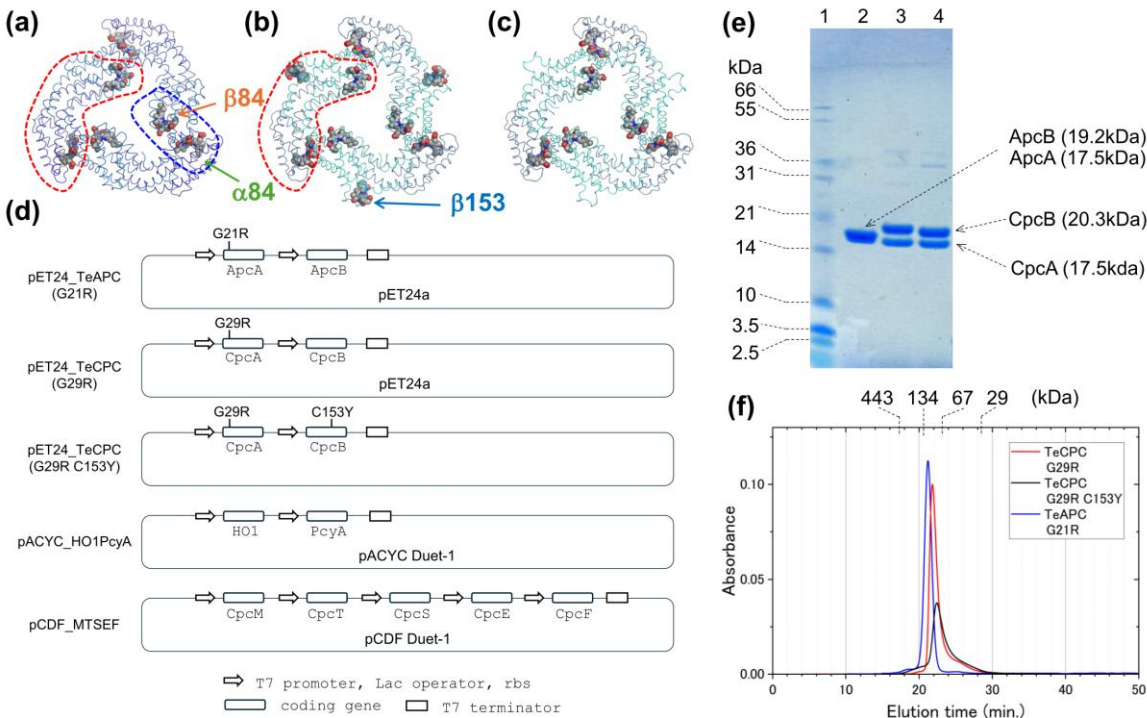


Fig. 1. Sample production and confirmation. (a-c) Structures of the wild-type APC trimer, wild-type CPC trimer, and β153-deficient CPC trimer, respectively. Phycocyanobilin (PCB) pigments at positions α84, β84, and β153 are shown using a van der Waals representation. The red dashed line indicates a monomer boundary. The blue dashed line surrounds a pair of pigments that form excitonic states. (d) Expression plasmids for protein synthesis. Three plasmids, pET24\_TeAPC G21R, pET24\_TeCPC G29R and pET24\_TeCPC G21R C153Y, were constructed to produce proteins shown in (a), (b), and (c), respectively. Co-expression plasmids pACYC\_HO1PcyA and pCDF\_MTSEF (for APC/CPC modification by encoded enzymes in *E. coli*) were also used.<sup>27</sup> (e) SDS-PAGE analysis. Lane 1: Mark12 Unstained Standard; Lanes 2-4: TeAPC G21R, TeCPC TeG29R, TeCPC G29R C153Y, respectively. (f) Size-exclusion column chromatography profiles. Arrows indicate elution times of standards: apoferitin (443 kDa, 17.32 min), dimer of bovine serum albumin (BSA) (134 kDa, 20.60 min), BSA (67 kDa, 23.14 min), and carbonic anhydrase (29 kDa, 28.50 min).

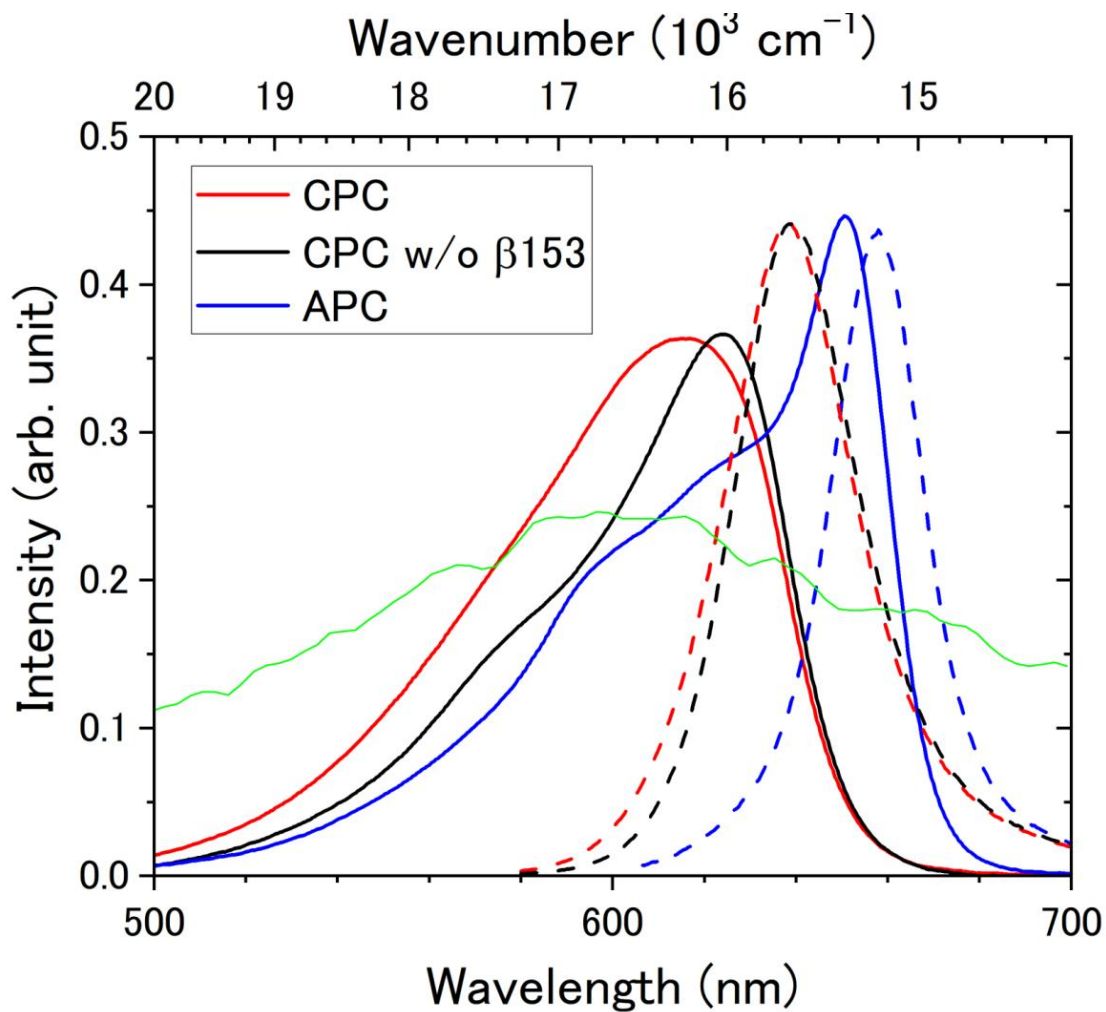


Fig. 2. Absorption and fluorescence spectra. The solid lines show the absorption spectra of APC (blue), CPC (red), and the  $\beta$ 153-deficient CPC (black). The fluorescence spectra shown as dashed lines were measured by the excitation light with the wavelength of 600 nm for APC and 570 nm for CPC and the mutant CPC. The thin green line represents the laser spectrum, which spans the entire absorption and fluorescence ranges of all proteins.

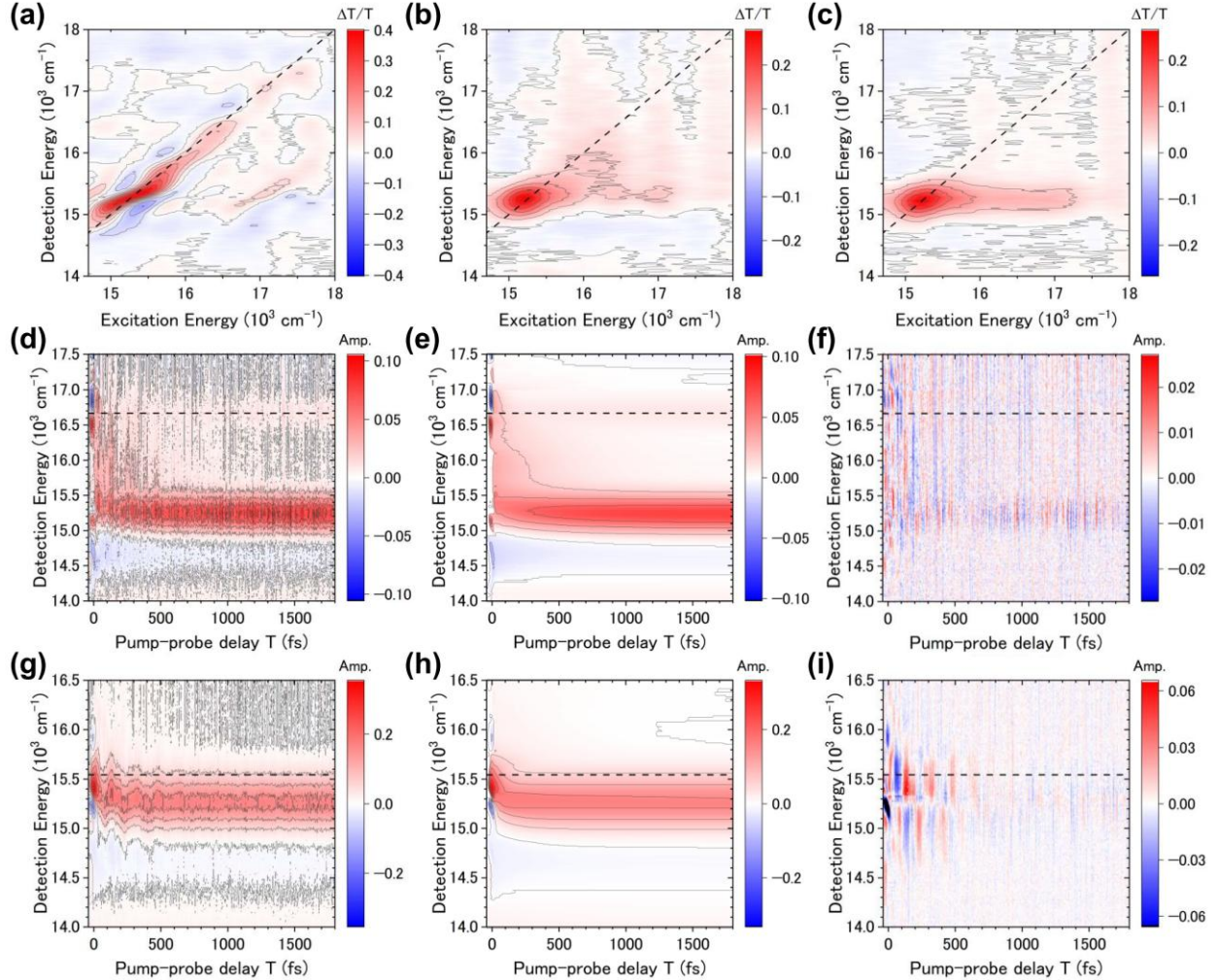


Fig. 3. 2D-E spectra  $S(E_{\text{exc}}, E_{\text{det}}; T)$  and transient spectra  $S(E_{\text{det}}, T; E_{\text{exc}})$  of APC. Panels (a-c) show the 2D-E spectra at pump-probe delay time  $T =$  (a) 0 fs, (b) 100 fs, and (c) 1 ps. The horizontal and vertical axes correspond to the excitation ( $E_{\text{exc}}$ ) and detection ( $E_{\text{det}}$ ) energies, respectively. Positive amplitudes indicate increased transmission, corresponding to GSB or SE, while negative amplitudes indicate ESA. The dashed line represents the diagonal. Panels (d) and (g) show the transient spectra obtained by slicing the three-dimensional data set of  $S(E_{\text{exc}}, E_{\text{det}}, T)$  at the excitation energies of  $E_{\text{exc}} = 16,670 \text{ cm}^{-1}$  and  $15,550 \text{ cm}^{-1}$ , respectively. These spectra are further separated to the (e, h) kinetic components and (f, i) coherent dynamics. The horizontal dashed lines in Panels (d-i) indicate the excitation energies.

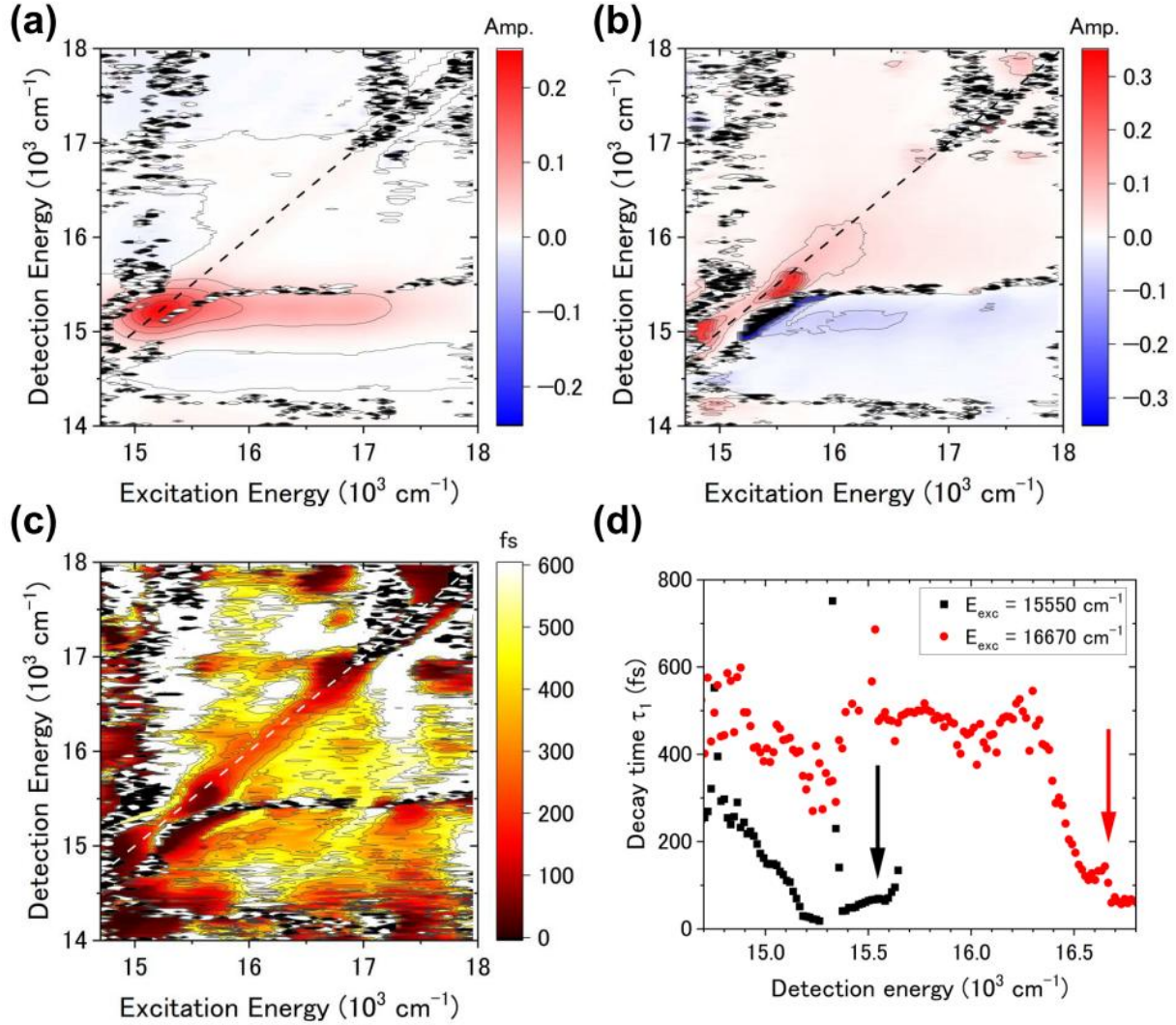


Fig. 4. Two-dimensional parameter maps of APC. The parameters (a)  $A_0$ , (b)  $A_1$ , and (c)  $\tau_1$  are derived from least-squares fitting to Eq.(1), respectively. The dashed line represents the diagonal. (d) Detection energy dependence of the time-constant  $\tau_1$  measured at the excitation energies of  $E_{\text{exc}} = 15,550 \text{ cm}^{-1}$  (black) and  $16,670 \text{ cm}^{-1}$  (red). The arrows show the excitation energies.

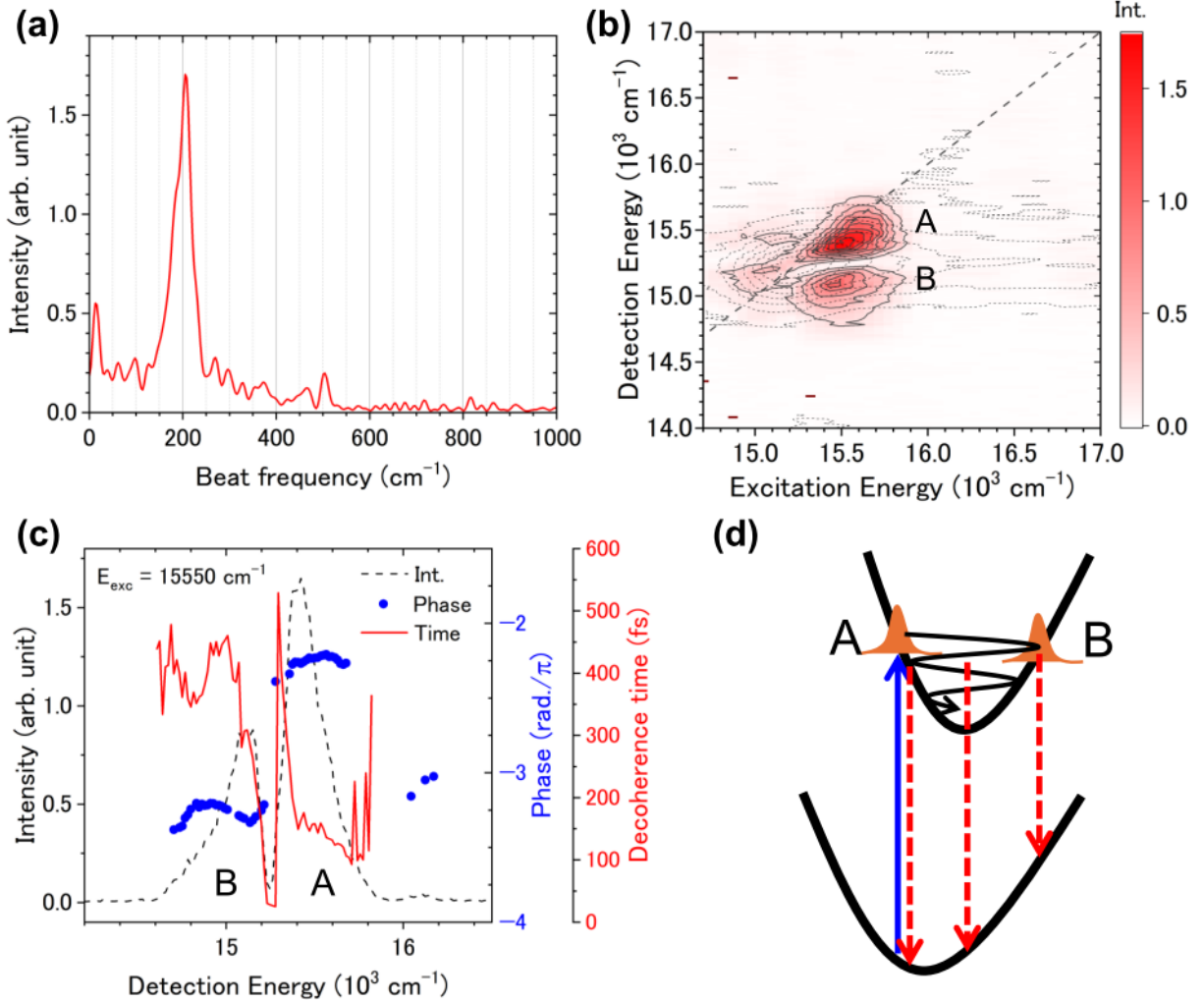


Fig. 5. (a) Beat frequency spectrum at an excitation energy of  $E_{\text{exc}} = 15,550 \text{ cm}^{-1}$ , averaged over detection energies in the range  $E_{\text{det}} = 15,000 \sim 15,650 \text{ cm}^{-1}$ . (b) Beat-frequency-resolved 2D-E spectra of APC averaged over beat frequencies  $\nu_{\text{beat}} = 202 \pm 46 \text{ cm}^{-1}$ . The dashed line indicates the diagonal. The 2D-E spectrum at  $T = 1 \text{ ps}$  is overlaid as the thin dashed contour map. (c) Beat intensity (black dashed line) and phase (blue circle dots) spectra at the excitation energy  $E_{\text{exc}} = 15,550 \text{ cm}^{-1}$ . Decoherence time as a function of the detection energy is also overlaid in this figure as the red solid line. (d) Schematic of vibrational wave packet on the electronically excited state.

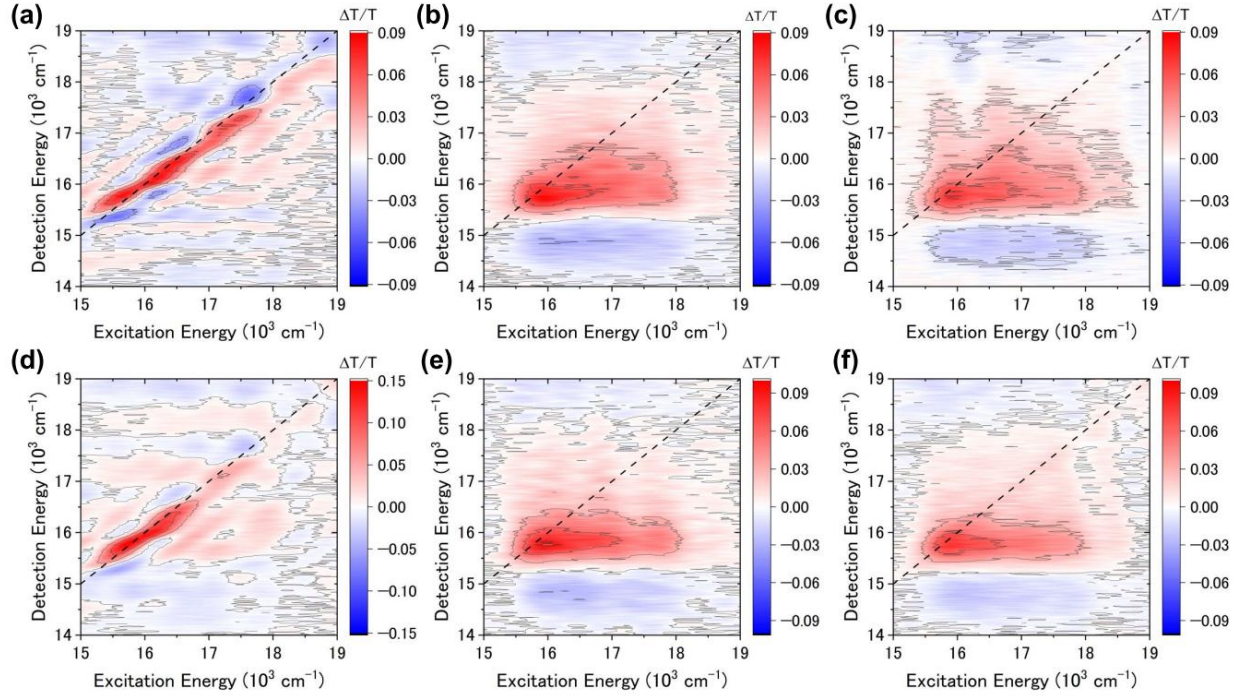


Fig. 6. A series of 2D-E spectra  $S(E_{\text{exc}}, E_{\text{det}}, T)$  of CPC and the mutant CPC. Panels (a-c) show the 2D-E spectra of CPC at the pump-probe delay time  $T =$  (a) 0 fs, (b) 100 fs, and (c) 1 ps. Panels (d-e) show the 2D-E spectra of the mutant CPC at  $T =$  (d) 0 fs, (e) 100 fs, and (f) 1 ps. The horizontal and vertical axes correspond to the excitation ( $E_{\text{exc}}$ ) and detection ( $E_{\text{det}}$ ) energies, respectively. Positive amplitudes indicate increased transmission, corresponding to GSB or SE, while negative amplitudes indicate ESA. The dashed line represents the diagonal.

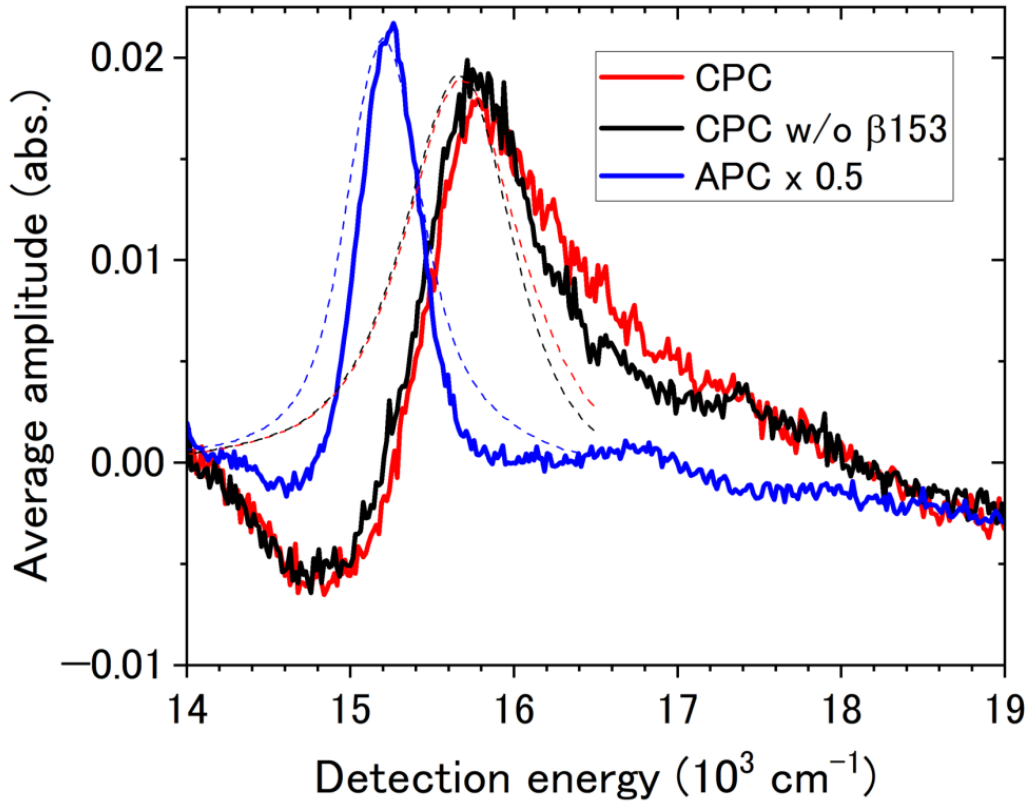


Fig. 7. Comparison between transient spectra (thick solid lines) at a long delay time ( $T = 2$  ps) and fluorescence spectra (thin dashed lines). The transient spectra are obtained by projecting the 2D-E spectra onto the detection energy axis. The red, black and blue lines represent the spectra of wild-type CPC, mutant CPC, and wild-type APC, respectively.

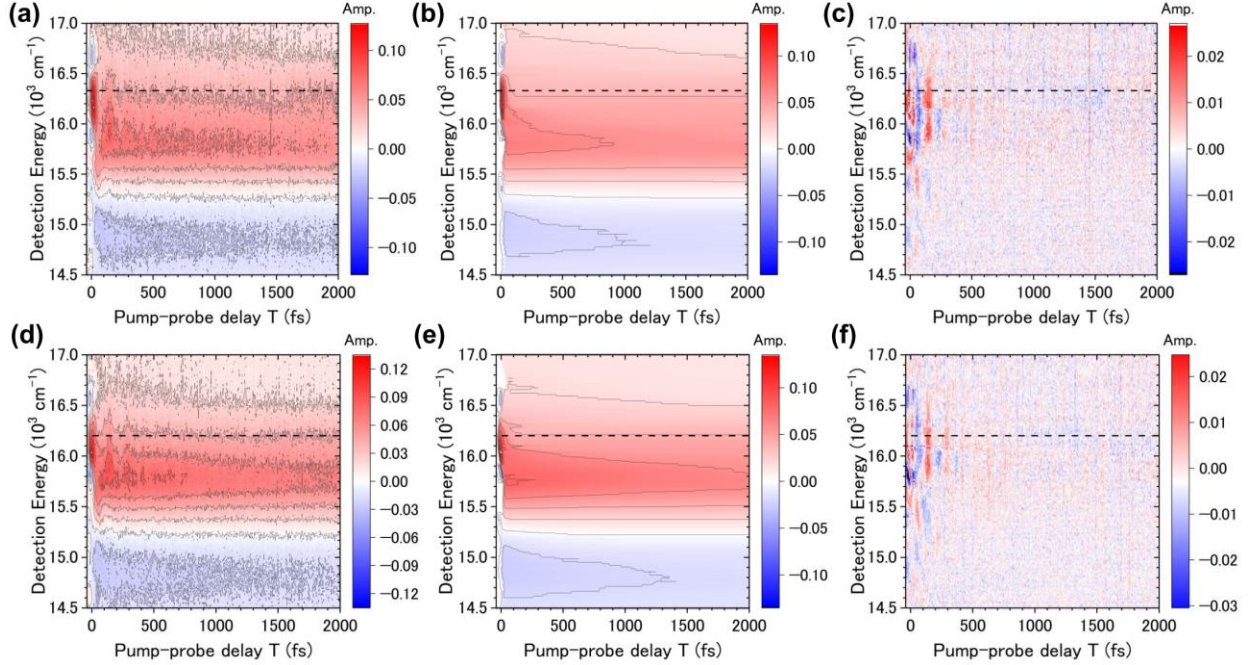


Fig. 8. Transient spectra  $S(E_{\text{det}}, T; E_{\text{exc}})$  of wild-type CPC and  $\beta 153$  deficient CPC. Panels (a) and (d) show the transient spectra of wild-type CPC and  $\beta 153$  deficient CPC obtained by slicing the three-dimensional data set of  $S(E_{\text{exc}}, E_{\text{det}}, T)$  at the excitation energies of  $E_{\text{exc}} = 16,330 \text{ cm}^{-1}$  and  $16,200 \text{ cm}^{-1}$ , respectively. These spectra are further separated to the (b, e) kinetic component and (c, f) coherent dynamics. The horizontal dashed lines indicate the excitation energies.

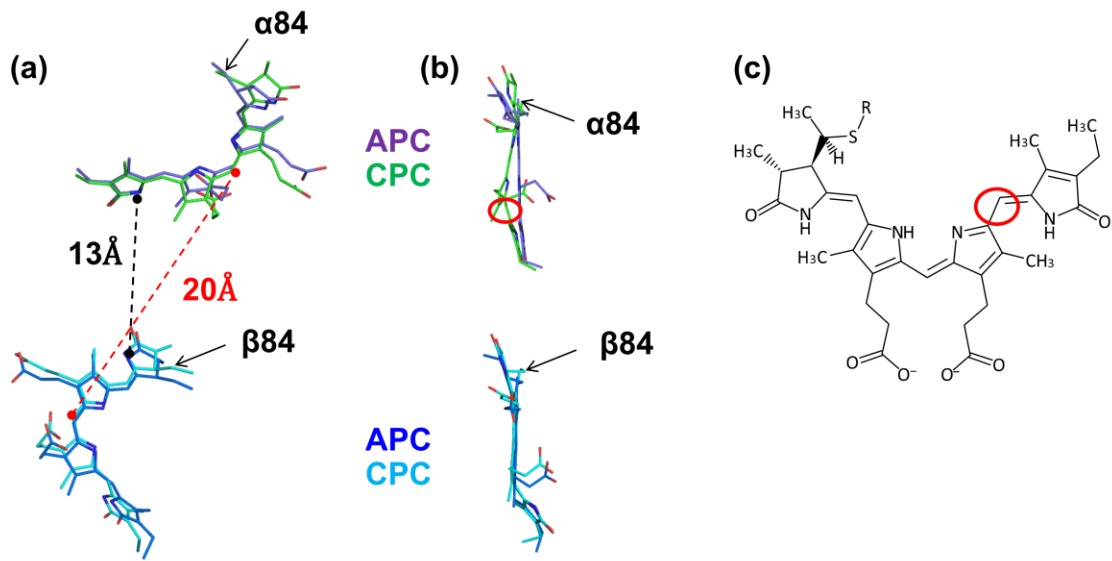


Fig. 9. Structures of phycocyanobilin (PCB) extracted from PDB entries 3DBJ and 3L0F, corresponding to wild-type APC and CPC, respectively. (a) Top view of PCB in the  $\alpha$ -chain (purple) and  $\beta$ -chain (blue) of APC, and the  $\alpha$ -chain (green) and  $\beta$ -chain (cyan) of CPC. Arrows indicate the binding site to the  $\alpha$ 84 and  $\beta$ 84 cysteine residues of proteins. (b) Side view of PCB, with relative positioning not preserved. (c) Structural formula of 3Z-Phycocyanobilin. The red circle highlights the C–C bond associated with structural difference in the  $\alpha$ 84 PCB between APC and CPC.

## Supplemental Issues

# **Roles of pigment arrangement in light-harvesting proteins revealed by artificial synthesis of allophycocyanin, C-phycoerythrin, and its mutant trimers combined with two-dimensional electronic spectroscopy**

**Masaaki Tsubouchi,<sup>1,2,a)</sup> Takatoshi Fujita,<sup>2</sup> Motoyasu Adachi,<sup>2</sup> and Ryuji Itakura<sup>1</sup>**

### **AFFILIATIONS**

<sup>1</sup>Kansai Institute for Photon Science (KPSI), National Institutes for Quantum Science and Technology (QST), 8-1-7 Umemidai, Kizugawa, Kyoto 619-0215, Japan

<sup>2</sup>Institute for Quantum Life Science, National Institutes for Quantum Science and Technology (QST), 4-9-1 Anagawa, Inage, Chiba 263-8555, Japan

<sup>a)</sup>Author to whom correspondence should be addressed: tsubouchi.masaaki@qst.go.jp

### **Contents**

1. Sample preparation
2. Analysis of two-dimensional electronic spectra
3. Analysis of vibrational wave packet
4. Transient spectra of CPC and the mutant CPC obtained at the higher excitation energy
5. Kinetics and coherence of CPC and the mutant CPC

References

## 1. Sample preparation

The recombinant proteins allophycocyanin (APC) and C-phycocyanin (CPC) from *Thermosynechococcus elongatus* BP-1 were independently produced by an *Escherichia coli* (*E. coli*) expression system. Supplementary Table S1 lists the expression plasmids used in this study. DNA and encoded amino acid sequences of proteins were deposited into the DNA Data Bank of Japan. The sequences were designed with a three-dimensional structure [1-6]. APC and CPC proteins typically assemble into hexameric structures of heterodimers of  $\alpha$ - and  $\beta$ -chains within the phycobilisome supercomplex. To facilitate spectroscopic and biochemical experiments, we introduced mutations at the intertrimeric interface to promote trimer formation.

The  $\alpha$ -chain of CPC and  $\alpha$ - and  $\beta$ -chains of APC link one phycocyanobilin (PCB) via a covalent bond as a pigment in native phycobilisome, whereas the  $\beta$ -chains of CPC link two PCBs. Two plasmids, pACYC\_HO1PcyA and pCDF\_MTSEF, were used for coexpression to enable pigment synthesis and protein modification, respectively. Specifically, Gly21 and Gly29 in the  $\alpha$ -chains of APC and CPC were substituted with arginine residues to introduce steric hindrances on the hexamer formation. Furthermore, to match the pigment configuration of CPC to that of APC, we generated a mutant CPC lacking the  $\beta$ 153 PCB pigment by substituting Cys153 with a tyrosine residue. The mutation of C153Y on pET\_TeCPC was introduced by PCR method using PrimeSTAR Max DNA Polymerase (Takara, Japan) and DNA primers of TeCPC\_C153Y\_F (5'-GGCGATTACAGCGCGCTGATGAGCGAAATC-3') and TeCPC\_C153Y\_R (5'-CGCGCTGTAATCGCCCGGGGTGATACCGTT-3'). Plasmids were prepared using QIAprep Spin Miniprep Kit (Qiagen). The DNA sequence coding for the protein was confirmed by DNA sequencing on the SeqStudio™ Genetic Analyzer (Thermo Fisher Scientific). In the following, unless otherwise specified, APC and CPC refer to the APC trimer and the CPC trimer, respectively. All DNAs were chemically synthesized and purchased from Genewiz (Azenta Life Sciences, Japan), and were optimized for *E. coli*. The expression plasmids were transfected into *E. coli* JM109(DE3) (Promega).

**Supplementary Table S1** | List of expression plasmids used in this study.

Name of plasmid Original plasmid	Coded proteins	Organisms*	Accession number (reference sequence)	Accession number deposited
pET_TeAPC (G21R) [APC]	pET24a (Novagen)	ApcA ApcB	BP-1 BP-1	NCBI: WP_011056801 NCBI: WP_011056800 LC912691
pET_TeCPC (G29R) [CPC]	pET24a (Novagen)	CpcA CpcB	BP-1 BP-1	NCBI: WP_011057793 NCBI: WP_011057792 LC912692
pET_TeCPC (G29R C153Y) [CPC]	pET24a (Novagen)	CpcA CpcB	BP-1 BP-1	NCBI: WP_011057793 NCBI: WP_011057792 Subcloned
pACYC_HO1PcyA [7]	pACYCDuet-1 (Novagen)	HO1 PcyA	6803 7120	NCBI: WP_010871494 NCBI: WP_010997850 LC853284
pCDF_MTSEF [7]	pCDFDuet-1 (Novagen)	CpcM	BP-1	NCBI: WP_011057783
		CpcT	7120	NCBI: WP_010999463
		CpcS	7120	NCBI: WP_010994793 LC853283
		CpcE	7120	NCBI: WP_010994708
		CpcF	7120	NCBI: WP_010994709

\*BP-1: *Thermosynechococcus elongatus* BP-1 (*Thermosynechococcus vestitus* BP-1)

6803: *Synechocystis* sp. PCC 6803

7120: *Nostoc* sp. 7120 (*Anabaena* sp.)

## 2. Analysis of two-dimensional electronic spectra

To understand the kinetics of the photoexcited molecules, Global analysis has been widely applied to the transient spectra. However, when coherent features overlap with kinetic components, applying Global analysis becomes difficult, because the experimental data cannot be accurately reconstructed using a small number of principal components obtained through singular value decomposition. Therefore, the time profiles obtained at all pairs of excitation and detection energies are fitted with a single exponential function,

$$S(T; E_{\text{exc}}, E_{\text{det}}) = A_0 + A_1 \exp(-T/\tau_1), \quad (\text{S1})$$

where  $E_{\text{exc}}$  and  $E_{\text{det}}$  are the excitation and detection energies, respectively.  $T$  is the delay time after photoexcitation.  $\tau_1$  is the time constant of the single exponential decay.  $A_0$  and  $A_1$  are the amplitudes of the constant and the decay components, respectively. These three parameters are the functions of  $E_{\text{exc}}$  and  $E_{\text{det}}$ .

In the fitting procedure, we also incorporate the instrumental response function (IRF) and account for the coherent artifact (CA) arising from non-resonant interactions between the pump and probe pulses near zero delay, as discussed in Refs [8, 9]. IRF is defined in Gaussian form as,

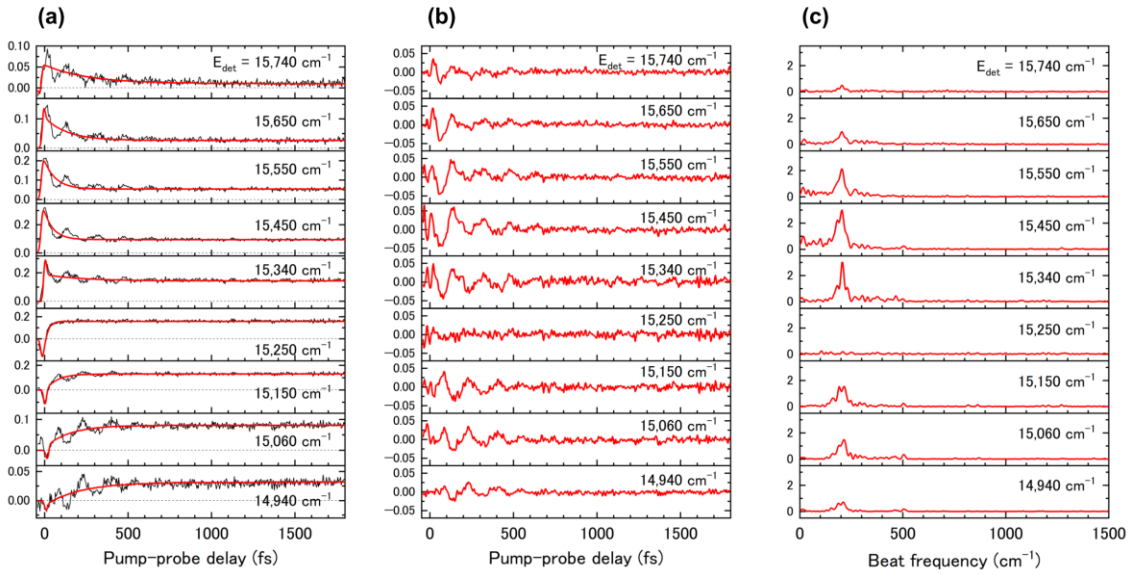
$$\text{IRF}(T) = \frac{1}{d\sqrt{2\pi}} \exp\left[-\frac{(T - T_0)^2}{2d^2}\right], \quad (\text{S2})$$

where  $T_0$  is the delay time corresponding to the IRF maximum, and  $d = \Delta/(2\sqrt{2 \ln 2})$  with  $\Delta$  representing the full width of half maximum (FWHM) of the IRF. This IRF function is convoluted with the exponential decay function Eq.(S1), and we obtain,

$$\begin{aligned} S(T; E_{\text{exc}}, E_{\text{det}}) * \text{IRF}(T) &= \frac{A_0}{2} \left[ 1 + \text{erf}\left(\frac{T - T_0}{d\sqrt{2}}\right) \right] \\ &+ \frac{A_1}{2} \left[ 1 + \text{erf}\left(\frac{T - T_0 - \frac{d^2}{\tau_1}}{d\sqrt{2}}\right) \right] \exp\left(-\frac{T}{\tau_1}\right) \exp\left(\frac{T_0 + \frac{d^2}{2\tau_1}}{\tau_1}\right). \end{aligned} \quad (\text{S3})$$

The CA component is described by the sum of the zeroth, first, and second derivatives of the IRF. The time profiles obtained at all pairs of excitation and detection energies are fitted with  $S(T; E_{\text{exc}}, E_{\text{det}}) * \text{IRF}(T) + \text{CA}(T)$ .

Supplementary Fig.1(a) shows the fitting results of the time profiles of wild-type APC using the model function described in this section. The profiles are obtained at an excitation energy of  $E_{\text{exc}} = 15,550 \text{ cm}^{-1}$ . The kinetic component and coherent dynamics are then separated based on the fitted profiles and their residuals, as shown in Supplementary Fig.1(b).



Supplementary Fig. 1. (a) Fitting results of the time profiles to the model function  $S(T; E_{\text{exc}}, E_{\text{det}}) * \text{IRF}(T) + \text{CA}(T)$ . The black and red lines represent the observed and the fitted profiles of wild-type APC at an excitation energy of  $E_{\text{exc}} = 15,550 \text{ cm}^{-1}$ . (b) Residual time profiles obtained by subtracting the fitted profiles from the observed ones. (c) Fourier-transformed spectra of the residual time profiles.

### 3. Analysis of vibrational wave packet

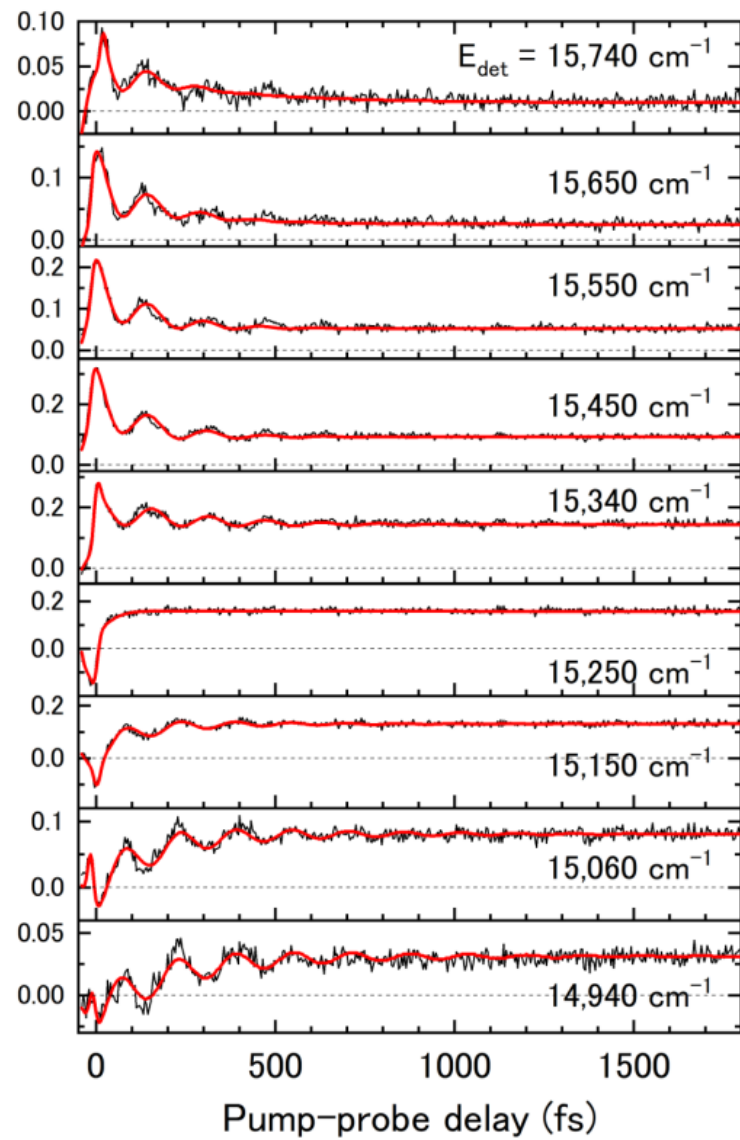
Supplementary Fig. 1(c) presents the Fourier-transformed spectra of the residual time profiles. A distinct peak is observed at the beat frequency  $\nu_{\text{beat}} = 202 \text{ cm}^{-1}$ . At the nodal line ( $E_{\text{det}} = 15,250 \text{ cm}^{-1}$ ) of the two-dimensional map shown in Fig. 5(b) of the main text, the amplitude of the beat spectrum decreases to zero.

To evaluate the decoherence time of the vibrational coherence at the beat frequency of  $202 \text{ cm}^{-1}$ , the observed time profiles are fitted to a single exponential decay function combined with a damped oscillation as follows. For this purpose, Eq.(S1) is modified as follows:

$$S_{\text{osc}}(T; E_{\text{exc}}, E_{\text{det}}) = S(T; E_{\text{exc}}, E_{\text{det}}) + A_{\text{osc}} \cos[2\pi\nu_{\text{beat}}(T - T_{\text{osc}})] \exp(-T/\tau_{\text{osc}}), \quad (\text{S4})$$

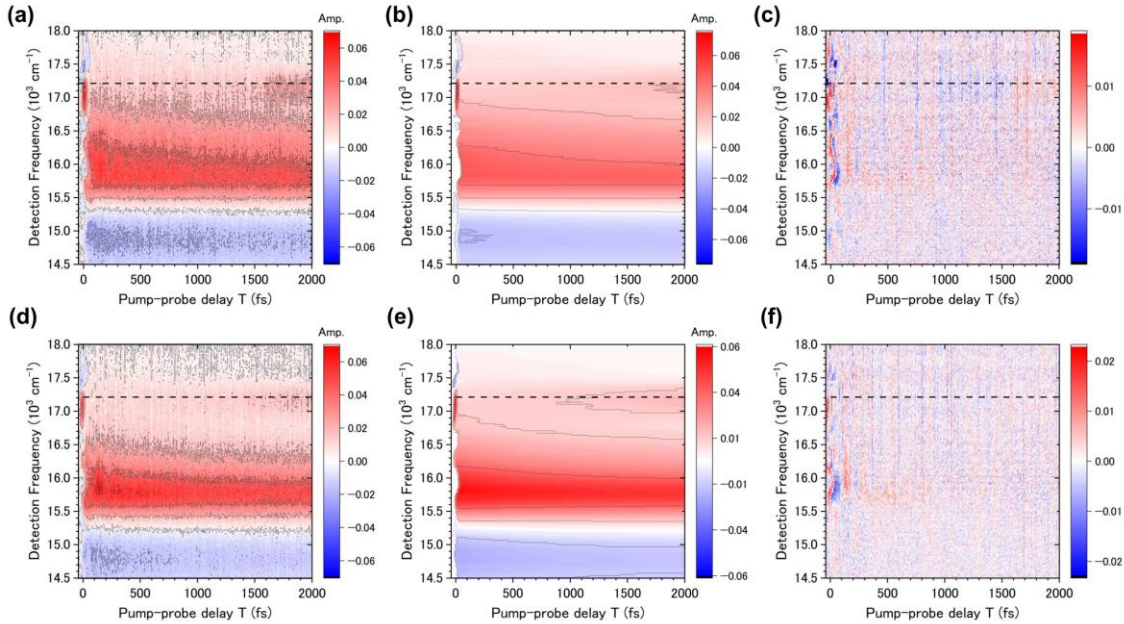
where  $A_{\text{osc}}$ ,  $T_{\text{osc}}$ , and  $\tau_{\text{osc}}$  represent the amplitude, phase delay, and decoherence time of the beat signal, respectively.

Supplementary Fig. 2 shows the fitting results of the time profiles of wild-type APC using the model function given in Eq.(S4). The profiles are obtained at an excitation energy of  $E_{\text{exc}} = 15,550 \text{ cm}^{-1}$ . The decoherence times determined from this fitting are presented in Fig. 5(c) of the main text as the red line.



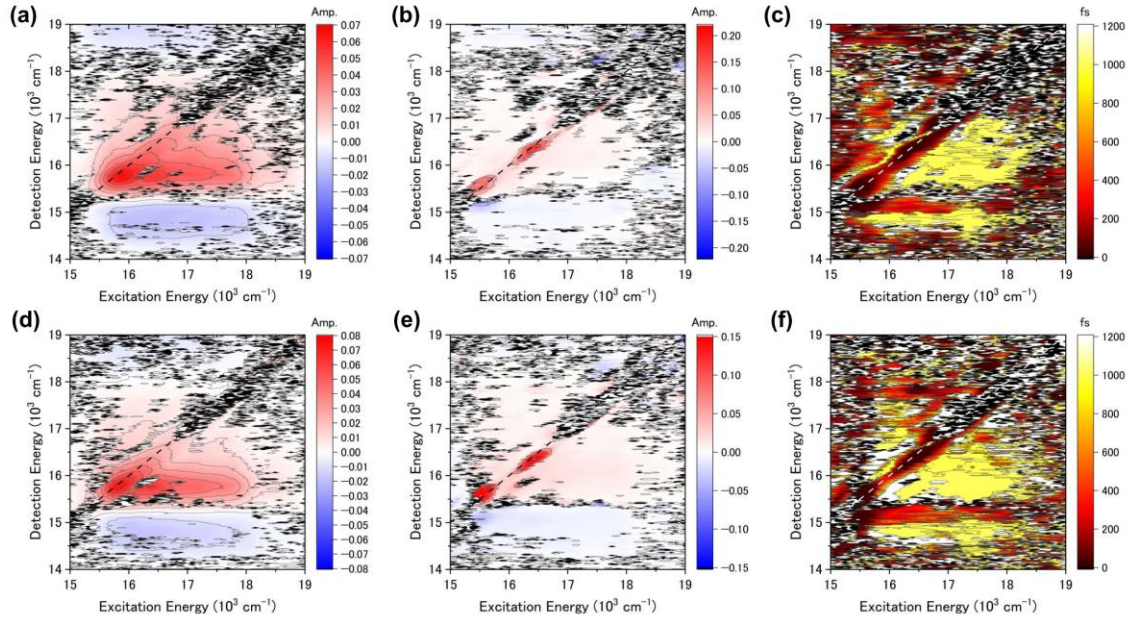
Supplementary Fig. 2. Fitting results of the time profiles to the model function of Eq.(S4). The black and red lines represent the observed and the fitted profiles of wild-type APC at an excitation energy of  $E_{\text{exc}} = 15,550 \text{ cm}^{-1}$ .

#### 4. Transient spectra of CPC and the mutant CPC obtained at the higher excitation energy



Supplementary Fig. 3. Transient spectra  $S(E_{\text{det}}, T; E_{\text{exc}})$  of wild-type CPC and  $\beta 153$  deficient CPC at the excitation energies of  $E_{\text{exc}} = 17, 210 \text{ cm}^{-1}$ . Panels (a) and (d) show the transient spectra of wild-type CPC and  $\beta 153$  deficient CPC obtained by slicing the three-dimensional data set of  $S(E_{\text{exc}}, E_{\text{det}}, T)$ , respectively. These spectra are further separated to the (b, e) kinetic component and (c, f) coherent dynamics. The horizontal dashed lines indicate the excitation energies.

## 5. Kinetics of CPC and the mutant CPC



Supplementary Fig. 4. Two-dimensional parameter maps of wild-type CPC and  $\beta 153$  deficient CPC. Panels (a-c) present the parameters  $A_0$ ,  $A_1$ , and  $\tau_1$  of wild-type CPC derived from least-squares fitting as described in Supplementary Sec. 2, respectively. Panels (d-f) present the parameters  $A_0$ ,  $A_1$ , and  $\tau_1$  of  $\beta 153$  deficient CPC, respectively. The dashed line represents the diagonal.

## References

1. K. Kawakami, T. Hamaguchi, Y. Hirose, D. Kosumi, M. Miyata, N. Kamiya, and K. Yonekura, "Core and rod structures of a thermophilic cyanobacterial light-harvesting phycobilisome," *Nat. Commun.* **13**, 3389 (2022).
2. A. McGregor, M. Klartag, L. David, and N. Adir, "Allophycocyanin trimer stability and functionality are primarily due to polar enhanced hydrophobicity of the phycocyanobilin binding pocket," *J. Mol. Biol.* **384**, 406-421 (2008).
3. W. Reuter, G. Wiegand, R. Huber, and M. E. Than, "Structural analysis at 2.2 Å of orthorhombic crystals presents the asymmetry of the allophycocyanin–linker complex, AP·L<sub>C</sub><sup>7.8</sup>, from phycobilisomes of *Mastigocladus laminosus*," *Proc. Natl. Acad. Sci. USA* **96**, 1363-1368 (1999).
4. J. Nield, P. J. Rizkallah, J. Barber, and N. E. Chayen, "The 1.45 Å three-dimensional structure of C-phycocyanin from the thermophilic cyanobacterium *Synechococcus elongatus*," *J. Mol. Biol.* **141**, 149-155 (2003).
5. L. David, A. Marx, and N. Adir, "High-resolution crystal structures of trimeric and rod phycocyanin," *J. Mol. Biol.* **405**, 201-213 (2011).
6. R. Fromme, A. Ishchenko, M. Metz, S. R. Chowdhury, S. Basu, S. Boutet, P. Fromme, T. A. White, A. Barty, J. C. H. Spence, U. Weierstall, W. Liu, and V. Cherezov, "Serial femtosecond crystallography of soluble proteins in lipidic cubic phase," *IUCrJ* **2**, 545-551 (2015).
7. M. Tsubouchi, N. Ishii, T. Fujita, M. Adachi, and R. Itakura, "Dependence of energy relaxation and vibrational coherence on the location of light-harvesting chromoproteins in photosynthetic antenna protein complexes," *J. Chem. Phys.* **162**(2025).
8. I. H. M. van Stokkum, C. C. Jumper, J. J. Snellenburg, G. D. Scholes, R. van Grondelle, and P. Malý, "Estimation of damped oscillation associated spectra from ultrafast transient absorption spectra," *The Journal of Chemical Physics* **145**(2016).
9. I. H. M. van Stokkum, M. Kloz, D. Polli, D. Viola, J. Weißenborn, E. Peerbooms, G. Cerullo, and J. T. M. Kennis, "Vibronic dynamics resolved by global and target analysis of ultrafast transient absorption spectra," *The Journal of Chemical Physics* **155**(2021).